IEEE Access
Multidisciplinary | Rapid Review | Open Access Journal

Received July 16, 2019, accepted August 10, 2019, date of publication August 13, 2019, date of current version August 28, 2019.

Digital Object Identifier 10.1109/ACCESS.2019.2935095

The Study on Near-Field Scattering of a Target Under Antenna Irradiation by TDSBR Method

GUANGBIN GUO, LIXIN GUO, (Senior Member, IEEE), AND RUI WANG
School of Physics and Optoelectronic Engineering, Xidian University, Xi'an 710071, China

Corresponding author: Lixin Guo (lxguo@mail.xidian.edu.cn)

This work was supported in part by the National Natural Science Foundation of China under Grant 61871457 and Grant 61431010, in part by the Foundation for Innovative Research Groups of the National Natural Science Foundation of China under Grant 61621005, in part by the National Natural Science Foundation of Shaanxi Province under Grant 2018JQ6045, in part by the Fundamental Research Funds for the Central Universities, and in part by the Innovation Fund of Xidian University.

ABSTRACT An efficient time domain shooting and bouncing ray (TDSBR) method is proposed to analyze the transient near-field scattering from an electrically large complex object illuminated by a far-field antenna source. The time-domain far-field incident sources can be derived by a convolution of pulsed excitation with the inverse Fourier transform of frequency domain (FD) far-fields radiated from an antenna. In order to obtain accurate near-field scattering results, time domain physical optics (TDPO) near-field integral representations are proposed and reduced to closed-form expressions to improve computing efficiency by applying locally expanded Green function approximation. Different from the plane wave incident situation, in the case of antenna radiation, the incident fields of each individual facet in the ray path are represented by the radiation fields from the equivalent mirror antenna derived in this paper. Since the radiation fields naturally contains the time delay term, the complicated processing of the time delay problem can be avoided by solving the equivalent mirror antenna radiation fields. It is simpler and more accurate than the traditional time domain geometrical optics (TDGO) method. Numerical examples are presented to demonstrate the efficiency and accuracy of the proposed method.

INDEX TERMS Time domain (TD), shooting and bouncing ray (SBR), near-field scattering, far-field antenna sources.

I. INTRODUCTION

With the widespread application of short-pulse communication and ultra-wideband radar systems in target detection, target recognition and remote sensing, the time-domain electromagnetic scattering analysis of targets has become one of the focuses in computational electromagnetics. There are many classical TD numerical methods such as finite-difference TD [1] or TD integral equation [2] approaches, which are all available to analyze the transient electromagnetic scattering from targets. However, as the electrical size of target increases, the computational time and resources required by TD numerical methods will become unbearable. In order to analyze the transient scattering of electrically large targets, a series of TD high-frequency methods which are generalized from the frequency domain (FD) high-frequency method are presented. Among these TD high-frequency methods, time domain physical optics (TDPO) is widely used to analyze transient electromagnetic scattering problems due to its fast computation speed and low memory consumption. In 1994, Sun and Rusch [3] first deduced the TDPO expression of the scattering far-field in the TD. The scattering field can be expressed as a surface integral of the equivalent electromagnetic current distribution on the scatterer based physical optics (PO) approximation. When using the numerical integration technique to evaluate the surface integral, in order to guarantee the accuracy of integral results, the integral step length is generally required to be no less than 1/5 wavelength and the calculation time will increases rapidly with an increase of the electrical size of scatterer. It is very time-consuming to calculate the scattering fields of electrically large targets. In FD, Gordon [4] reduced the far-field PO surface integral on a flat polygonal to a closed-form expression to improve the computational efficiency. Zhou and Cui [5] derived the corresponding TD expression in direct TD. However, these closed-form

The associate editor coordinating the review of this article and approving it for publication was Chan Hwang See.

representations in TD and FD can only be available if the observation point is located at infinity. For near-field scattering, the traditional far-field assumption seriously reduces the calculation accuracy when simulating the scattering field close to the scatterer. In order to obtain accurate near-field scattering results, Legault [6] presented an accurate and efficient approach that relies on a phase approximation of the same order as the one used in the far-field close-form formulas. Inspired by Legault's method, Zhou and Cui [7] derived the TDPO surface integral expressions of scattering near-fields and reduced the surface integral expressions on a flat polygonal to closed-form expressions under pulsed plane wave incident. Some other work focuses on transforming the surface integrals into line integrals without loss of precision. The line integral is mainly used to analyze near field scattering. Fan *et al.* [8] developed a TDPO line-integral representation for the scattering from a perfectly conducting surface illuminated by an electric Hertzian dipole. The advantage of the line integral expression is that it has the same precision as the surface integral expression. However, because the numerical integration technique is needed to evaluate the line integral, the calculation efficiency of the line integral is lower than that of the closed-form expression. Since the PO method fails to consider the reflection fields in the target, the single PO method cannot provide an accurate prediction when a complex target is analyzed.

In 1980, Whitted [9], Rubin and Whitted [10] proposed a ray-tracing (RT) algorithm for high-resolution two-dimensional display of three-dimensional scenes. In 1989, Ling *et al.* [11] introduced RT algorithm into electromagnetic computing and proposed SBR to predict electromagnetic scattering of complex targets. When SBR is used to evaluate electromagnetic scattering of targets, the incident field of the irradiated surface is determined by GO, and the scattering field is generally calculated by PO integral on the illuminated area. Since the SBR method was proposed, many scholars have been committed to the research of SBR method, including improving the computational efficiency and accuracy and extending the application range. The key factor affecting the computational efficiency of SBR algorithm is the intersecting operation between a large number of ray beams and the target. To improve the computational efficiency of SBR algorithm, Suk *et al.* [12] introduced a multi-resolution grid algorithm to reduce the number of initial ray tubes. Jin *et al.* [13] used the octree structure to reduces the complexity of intersection between ray and target. Bang *et al.* [14] further improved the computational efficiency by mixing the multi-resolution grid algorithm and the spatial partitioning acceleration algorithm. Fan and Guo [15] introduced the graphical programming interface Open Graphics Library (OpenGL) to the SBR algorithm and further improved the computational efficiency of the SBR by using some acceleration techniques such as double buffering, display list and vertex cache. In 2016, Fan *et al.* [16] combines kd-tree and bidirectional tracking technology to improve the efficiency of ray intersection. Jeng [17] proposed a hybrid method of SBR and PTD to compute the near-field radar cross section (RCS) and Doppler spectrum of a target when both the radiation source and the receiver source are antennas. Guo and Guo [18] used SBR method to solve near-field scattering of an electrically large complex target illuminated by dipole sources. In the time domain, Ling and Bhalla [19] proposed a time-domain version SBR method (TDSBR) based on the classical FD SBR algorithm in 1993. In [19], they derived a closed-form TD ray tube integral expression to rapidly calculate the TD response of complex targets. By summing the contributions of each ray in the time domain, the whole time domain response of the target can be obtained. Bhalla and Ling [20] then extended TDSBR to imaging simulation of inverse synthetic range aperture radar (ISAR). In 2015, Zhou *et al.* [21] presented a TDSBR method based on the beam tracing (BT) technique [22]–[24] to analyze the transient scattering responses from large PEC objects illuminated by a pulsed plane wave. However, the BT technique can only solve the situation where the radiation source is a plane wave. Although there are many researches on the SBR method to analyze the near-field scattering under antenna radiation in frequency domain, there are few studies on the TD transient scattering. At present, the researches on TDSBR are mainly about far-field transient scattering under the incident pulse plane wave and it has not been reported that TDSBR is used to analyze the near-field transient scattering responses under the antenna irradiation.

In practical applications, for electrically large targets, the receiving antenna is usually located in the scattered near-field region of the target and the radiation field of the transmitting antenna is not plane wave but far-field beam. A large number of studies have shown that, different from the far-field scattering characteristics, the antenna motion, the antenna pattern and the local irradiation, will seriously affect the near-field scattering characteristics of the target, thus affecting the detection and recognition of the target. So, it is necessary to study the near-field scattering of the target illuminated by a far-field antenna. In this paper, inspired by Zhou and Cui [7], TDPO near-field integral representations are proposed and reduced to closed form expressions to investigate the transient scattered near-fields from targets illuminated by far-field antenna sources. The main point of this approach is that the surface of target is meshed densely enough and each individual facet is small enough that the antenna is in the far-field region of the facet. Then each facet can be treated as a new small object and the scattering fields of each facet can be obtained by far-field assumption. The total fields of an object can be obtained by adding the scattering fields of all facet.

In addition, in the process of tracking the reflected field value, we propose an equivalent mirror antenna method to replace the traditional GO. Different from the plane wave incident situation, in the case of antenna radiation, we obtain the incident fields of each individual facet in the ray path by solving the radiation fields of the equivalent mirror antenna. Since the radiation fields naturally contains the time delay term, the complicated processing of the time delay problem

can be avoided by solving the radiation fields from equivalent mirror antenna.

The remainder of this paper is organized as follows. Section II discusses the derivation of the near-field TDPO closed-form expressions. Section III describes the simple concept of equivalent image antenna. Section IV provides numerical examples. Section V discusses the conclusion drawn from this study.

II. DERIVATION OF NEAR-FIELD TDPO CLOSED-FORM EXPRESSIONS

As shown in Fig. 1, an arbitrarily shaped plate S with the unit vector normal $\hat{\boldsymbol{n}}$ is illuminated by an antenna located at $\boldsymbol{r}_s$. The receiving antenna is at point P with position vector $\boldsymbol{r}$. $\boldsymbol{r}'$ denotes a point on the plate S. $\boldsymbol{R} = \boldsymbol{r} - \boldsymbol{r}'$ and $\boldsymbol{\rho} = \boldsymbol{r}' - \boldsymbol{r}_s$. In FD, the radiation far-fields of an antenna can be expressed as [25]:

$$\boldsymbol{E}_i(\boldsymbol{r}', \omega) = -j\eta k \frac{\exp(-jk\rho)}{4\pi\rho} \boldsymbol{f}(\theta, \varphi) \tag{1}$$

$$\boldsymbol{H}_i(\boldsymbol{r}', \omega) = \frac{1}{\eta} \hat{\boldsymbol{\rho}} \times \boldsymbol{E}_i(\boldsymbol{r}', \omega) \tag{2}$$

where, $\boldsymbol{f}(\theta, \varphi)$ is the vector current moment. η denotes the free-space intrinsic impedance. ρ denotes the magnitude of $\boldsymbol{\rho}$ and $\hat{\boldsymbol{\rho}} = \boldsymbol{\rho}/\rho$.

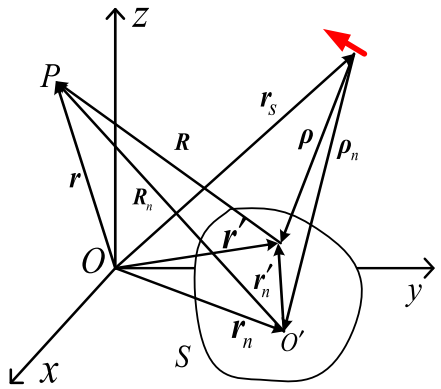

FIGURE 1. Geometry of the scattering by a perfectly conducting flat surface illuminated by an antenna.

Next, let $\boldsymbol{F}(\theta, \varphi) = -jk\boldsymbol{f}(\theta, \varphi)$. Taking the inverse Fourier transform of (1) and (2), the transient radiation far-fields from an antenna with excitation pulse $p(t)$ can be given by the following:

$$\begin{aligned}\boldsymbol{E}_i(\boldsymbol{r}', t) &= p(t) * \mathbb{F}^{-1}\left[\boldsymbol{E}_i(\boldsymbol{r}', \omega)\right] \\ &= \frac{\eta}{4\pi\rho} p(t) * \mathbb{F}^{-1}\left[\boldsymbol{F}(\theta, \varphi)\right] * \delta\left(t - \frac{\rho}{c}\right)\end{aligned} \tag{3}$$

$$\boldsymbol{H}_i(\boldsymbol{r}', t) = \frac{1}{\eta} \hat{\boldsymbol{\rho}} \times \boldsymbol{E}_i(\boldsymbol{r}', t) \tag{4}$$

$\delta(t)$ is the impulse function. c refers to the speed of light in free-space. "$*$" denotes the convolution operation. $\mathbb{F}^{-1}$ denotes the inverse Fourier transform.

In accordance with the surface integral equations of the electromagnetic fields in the TD presented in [26], the TDPO scattering near-fields of the plate S can be expressed as:

$$\begin{aligned}\boldsymbol{E}_s(\boldsymbol{r}, t) = \frac{1}{4\pi} \int_S \Bigg\{ &\hat{\boldsymbol{R}} \times \left[\frac{R}{c}\boldsymbol{M}(\boldsymbol{r}', t) + \boldsymbol{M}^{(-1)}(\boldsymbol{r}', t)\right] \\ &+\eta \left[\left(\boldsymbol{J}^{(-1)}(\boldsymbol{r}', t) + \frac{c}{R}\boldsymbol{J}^{(-2)}(\boldsymbol{r}', t)\right) \cdot \left(3\hat{\boldsymbol{R}}\hat{\boldsymbol{R}} - \bar{\bar{\boldsymbol{I}}}\right)\right. \\ &\left. + \frac{R}{c}\boldsymbol{J}(\boldsymbol{r}', t) \cdot (\hat{\boldsymbol{R}}\hat{\boldsymbol{R}} - \bar{\bar{\boldsymbol{I}}})\right] \Bigg\} * \frac{\delta'(t - R/c)}{R^2} dS'\end{aligned} \tag{5}$$

$$\begin{aligned}\boldsymbol{H}_s(\boldsymbol{r}, t) = \frac{1}{4\pi} \int_S \Bigg\{ &\left[\frac{R}{c}\boldsymbol{J}(\boldsymbol{r}', t) + \boldsymbol{J}^{(-1)}(\boldsymbol{r}', t)\right] \times \hat{\boldsymbol{R}} \\ &+\frac{1}{\eta} \left[\left(\boldsymbol{M}^{(-1)}(\boldsymbol{r}', t) + \frac{c}{R}\boldsymbol{M}^{(-2)}(\boldsymbol{r}', t)\right) \cdot \left(3\hat{\boldsymbol{R}}\hat{\boldsymbol{R}} - \bar{\bar{\boldsymbol{I}}}\right)\right. \\ &\left. + \frac{R}{c}\boldsymbol{M}(\boldsymbol{r}', t) \cdot (\hat{\boldsymbol{R}}\hat{\boldsymbol{R}} - \bar{\bar{\boldsymbol{I}}})\right] \Bigg\} * \frac{\delta'(t - R/c)}{R^2} dS'\end{aligned} \tag{6}$$

and

$$\begin{aligned}\boldsymbol{J}(\boldsymbol{r}', t) &= \hat{\boldsymbol{n}} \times \boldsymbol{H}(\boldsymbol{r}', t) \\ &= \hat{\boldsymbol{n}} \times \left[\boldsymbol{H}_i(\boldsymbol{r}', t) + \boldsymbol{H}_r(\boldsymbol{r}', t)\right] \\ \boldsymbol{J}^{(-1)}(\boldsymbol{r}', t) &= \int_{t_0}^{t} \boldsymbol{J}(\boldsymbol{r}', t')\, dt' \\ \boldsymbol{J}^{(-2)}(\boldsymbol{r}', t) &= \int_{t_0}^{t} \boldsymbol{J}^{(-1)}(\boldsymbol{r}', t')\, dt'\end{aligned} \tag{7}$$

$$\begin{aligned}\boldsymbol{M}(\boldsymbol{r}', t) &= -\hat{\boldsymbol{n}} \times \boldsymbol{E}(\boldsymbol{r}', t) \\ &= -\hat{\boldsymbol{n}} \times \left[\boldsymbol{E}_i(\boldsymbol{r}', t) + \boldsymbol{E}_r(\boldsymbol{r}', t)\right] \\ \boldsymbol{M}^{(-1)}(\boldsymbol{r}', t) &= \int_{t_0}^{t} \boldsymbol{M}(\boldsymbol{r}', t')\, dt' \\ \boldsymbol{M}^{(-2)}(\boldsymbol{r}', t) &= \int_{t_0}^{t} \boldsymbol{M}^{(-1)}(\boldsymbol{r}', t')\, dt'\end{aligned} \tag{8}$$

In these expressions above, R denotes the magnitude of $\boldsymbol{R}$ and $\hat{\boldsymbol{R}} = \boldsymbol{R}/R$. $\delta'(t)$ is the first-order derivative of the delta function. $\boldsymbol{H}_i(\boldsymbol{r}', t)$, $\boldsymbol{E}_i(\boldsymbol{r}', t)$ and $\boldsymbol{H}_r(\boldsymbol{r}', t)$, $\boldsymbol{E}_r(\boldsymbol{r}', t)$ denote the incident fields and reflection fields on surface S, respectively. t_0 is a finite initial moment and the incident fields are 0 when $t < t_0$.

Suppose that plate S is a small cell subdivided from the surface of target. If the size D of S is small enough to satisfy both $2D^2/\lambda_{\min} \ll |\boldsymbol{r} - \boldsymbol{r}'|$ and $2D^2/\lambda_{\min} \ll |\boldsymbol{r}_s - \boldsymbol{r}'|$ for any point $\boldsymbol{r}'$ on S ($\lambda_{\min}$ is the wavelength according to the maximum frequency of the incident wave), then the far-field approximation can be applied in this case [17] and the incident fields at $\boldsymbol{r}'$ can be represented by far-fields radiated from transmitting antenna. Let O' be the center of plate S and denote the position vector of the center as $\boldsymbol{r}_n$. Apply the far-field approximation $\rho = |\boldsymbol{r}' - \boldsymbol{r}_s| \approx \rho_n$ for magnitude and $\rho = |\boldsymbol{r}' - \boldsymbol{r}_s| \approx \hat{\boldsymbol{\rho}}_n \cdot (\boldsymbol{r}' - \boldsymbol{r}_s)$ for time delay, where $\rho_n = |\boldsymbol{r}_n - \boldsymbol{r}_s|$ and $\hat{\boldsymbol{\rho}} \approx \hat{\boldsymbol{\rho}}_n = (\boldsymbol{r}_n - \boldsymbol{r}_s)/\rho_n$. The incident fields on the plate S can be rewritten as:

$$\begin{aligned}\boldsymbol{E}_i(\boldsymbol{r}', t) = &\frac{\eta}{4\pi\rho_n} p(t) * \mathbb{F}^{-1}\left[\boldsymbol{F}(\theta, \varphi)\right] \\ &* \delta\left(t + \frac{\hat{\boldsymbol{\rho}}_n \cdot \boldsymbol{r}_s}{c} - \frac{\hat{\boldsymbol{\rho}}_n \cdot \boldsymbol{r}'}{c}\right)\end{aligned} \tag{9}$$

$$\boldsymbol{H}_i(\boldsymbol{r}', t) = \frac{1}{\eta} \hat{\boldsymbol{\rho}}_n \times \boldsymbol{E}_i(\boldsymbol{r}', t) \tag{10}$$

It can be seen from the formula (9) that the incident field can be expressed as the convolution of the pulsed excitation $p(t)$ with an impulse plane wave. This enables us to approximate the incident field on each facet as a local plane wave with different magnitude. Based on this approximation, $\boldsymbol{H}_r(\boldsymbol{r}', t)$ in formula (7) and $\boldsymbol{E}_r(\boldsymbol{r}', t)$ in formula (8) can be expressed as:

$$\begin{aligned}\boldsymbol{H}_r(\boldsymbol{r}', t) &= R_{TE}\left[\boldsymbol{H}_i(\boldsymbol{r}', t)\cdot -\hat{\boldsymbol{e}}_{TM}\right]\left(\hat{\boldsymbol{k}}_r\times\hat{\boldsymbol{e}}_{TE}\right)\\ &\quad + R_{TM}\left[\boldsymbol{H}_i(\boldsymbol{r}', t)\cdot\hat{\boldsymbol{e}}_{TE}\right]\hat{\boldsymbol{e}}_{TE} \qquad (11)\\ \boldsymbol{E}_r(\boldsymbol{r}', t) &= R_{TE}\left[\boldsymbol{E}_i(\boldsymbol{r}', t)\cdot\hat{\boldsymbol{e}}_{TE}\right]\hat{\boldsymbol{e}}_{TE}\\ &\quad + R_{TM}\left[\boldsymbol{E}_i(\boldsymbol{r}', t)\cdot\hat{\boldsymbol{e}}_{TM}\right]\left(\hat{\boldsymbol{e}}_{TE}\times\hat{\boldsymbol{k}}_r\right) \qquad (12)\end{aligned}$$

where R_{TM} and $\hat{\boldsymbol{e}}_{TM}$ denote the reflection coefficients and normalized direction of TM wave. R_{TE} and $\hat{\boldsymbol{e}}_{TE}$ denote the reflection coefficients and normalized direction of TE wave. $\hat{\boldsymbol{k}}_r$ is the reflection direction as follows:

$$\hat{\boldsymbol{k}}_r = \hat{\boldsymbol{\rho}}_n - 2\hat{\boldsymbol{n}}\left(\hat{\boldsymbol{\rho}}_n\cdot\hat{\boldsymbol{n}}\right) \qquad (13)$$

By substituting (11)-(13) into (7) and (8), $\boldsymbol{J}(\boldsymbol{r}', t)$ and $\boldsymbol{M}(\boldsymbol{r}', t)$ can be represented by the incident fields and $\hat{\boldsymbol{n}}$:

$$\begin{aligned}\boldsymbol{J}(\boldsymbol{r}', t) &= \hat{\boldsymbol{n}}\times\boldsymbol{H}(\boldsymbol{r}', t)\\ &= (1-R_{TE})\left[\boldsymbol{H}_i(\boldsymbol{r}', t)\cdot\hat{\boldsymbol{e}}_{TM}\right]\left(\hat{\boldsymbol{\rho}}_n\cdot\hat{\boldsymbol{n}}\right)\hat{\boldsymbol{e}}_{TE}\\ &\quad + (1+R_{TM})\left[\boldsymbol{H}_i(\boldsymbol{r}', t)\cdot\hat{\boldsymbol{e}}_{TE}\right]\left(\hat{\boldsymbol{n}}\times\hat{\boldsymbol{e}}_{TE}\right) \qquad (14)\\ \boldsymbol{M}(\boldsymbol{r}', t) &= -\hat{\boldsymbol{n}}\times\boldsymbol{E}(\boldsymbol{r}', t)\\ &= (1-R_{TM})\left[\boldsymbol{E}_i(\boldsymbol{r}', t)\cdot\hat{\boldsymbol{e}}_{TM}\right]\left(-\hat{\boldsymbol{\rho}}_n\cdot\hat{\boldsymbol{n}}\right)\hat{\boldsymbol{e}}_{TE}\\ &\quad + (1+R_{TE})\left[\boldsymbol{E}_i(\boldsymbol{r}', t)\cdot\hat{\boldsymbol{e}}_{TE}\right]\left(\hat{\boldsymbol{e}}_{TE}\times\hat{\boldsymbol{n}}\right) \qquad (15)\end{aligned}$$

Then, apply the far-field approximation $R = |\boldsymbol{r}-\boldsymbol{r}'| \approx R_n$ for magnitude and $R = |\boldsymbol{r}-\boldsymbol{r}'| \approx \hat{\boldsymbol{R}}_n\cdot(\boldsymbol{r}-\boldsymbol{r}')$ for time delay, where $R_n = |\boldsymbol{r}-\boldsymbol{r}_n|$ and $\hat{\boldsymbol{R}} \approx \hat{\boldsymbol{R}}_n = (\boldsymbol{r}-\boldsymbol{r}_n)/R_n$. The scattering fields $\boldsymbol{E}_s(\boldsymbol{r},t)$ and $\boldsymbol{H}_s(\boldsymbol{r},t)$ can be derived as:

$$\begin{aligned}\boldsymbol{E}_s(\boldsymbol{r},t) &= \frac{\eta}{16\pi^2\rho_n R_n^2}\left\{\hat{\boldsymbol{R}}_n\times\left[\frac{R_n}{c}\boldsymbol{M}_a(t)+\boldsymbol{M}_a^{(-1)}(t)\right]\right.\\ &\quad + \frac{R_n}{c}\boldsymbol{J}_a(t)\cdot(\hat{\boldsymbol{R}}_n\hat{\boldsymbol{R}}_n-\bar{\bar{\boldsymbol{I}}})\\ &\quad \left.+\left(\boldsymbol{J}_a^{(-1)}(t)+\frac{c}{R_n}\boldsymbol{J}_a^{(-2)}(t)\right)\cdot\left(3\hat{\boldsymbol{R}}_n\hat{\boldsymbol{R}}_n-\bar{\bar{\boldsymbol{I}}}\right)\right\}\\ &\quad *\delta\left(t-\frac{\hat{\boldsymbol{R}}_n\cdot\boldsymbol{r}-\hat{\boldsymbol{\rho}}_n\cdot\boldsymbol{r}_s}{c}\right)\\ &\quad *\int_S\delta'\left(t-\frac{\left(\hat{\boldsymbol{\rho}}_n-\hat{\boldsymbol{R}}_n\right)\cdot\boldsymbol{r}'}{c}\right)dS' \qquad (16)\end{aligned}$$

$$\begin{aligned}\boldsymbol{H}_s(\boldsymbol{r},t) &= \frac{1}{16\pi^2\rho_n R_n^2}\left\{\left[\frac{R_n}{c}\boldsymbol{J}_a(t)+\boldsymbol{J}_a^{(-1)}(t)\right]\times\hat{\boldsymbol{R}}_n\right.\\ &\quad + \frac{R_n}{c}\boldsymbol{M}_a(t)\cdot(\hat{\boldsymbol{R}}_n\hat{\boldsymbol{R}}_n-\bar{\bar{\boldsymbol{I}}})\\ &\quad \left.+\left(\boldsymbol{M}_a^{(-1)}(t)+\frac{c}{R_n}\boldsymbol{M}_a^{(-2)}(t)\right)\cdot\left(3\hat{\boldsymbol{R}}_n\hat{\boldsymbol{R}}_n-\bar{\bar{\boldsymbol{I}}}\right)\right\}\\ &\quad *\delta\left(t-\frac{\hat{\boldsymbol{R}}_n\cdot\boldsymbol{r}-\hat{\boldsymbol{\rho}}_n\cdot\boldsymbol{r}_s}{c}\right)\\ &\quad *\int_S\delta'\left(t-\frac{\left(\hat{\boldsymbol{\rho}}_n-\hat{\boldsymbol{R}}_n\right)\cdot\boldsymbol{r}'}{c}\right)dS' \qquad (17)\end{aligned}$$

where

$$\begin{aligned}\boldsymbol{J}_{\mathrm{a}}^{(-n)}(t) &= (1-R_{TE})\left[\boldsymbol{h}_i^{(-n)}(t)\cdot\hat{\boldsymbol{e}}_{TM}\right]\left(\hat{\boldsymbol{\rho}}_n\cdot\hat{\boldsymbol{n}}\right)\hat{\boldsymbol{e}}_{TE}\\ &\quad + (1+R_{TM})\left[\boldsymbol{h}_i^{(-n)}(t)\cdot\hat{\boldsymbol{e}}_{TE}\right]\left(\hat{\boldsymbol{n}}\times\hat{\boldsymbol{e}}_{TE}\right) \qquad (18)\\ \boldsymbol{M}_a^{(-n)}(t) &= (1-R_{TM})\left[\boldsymbol{e}_i^{(-n)}(t)\cdot\hat{\boldsymbol{e}}_{TM}\right]\left(-\hat{\boldsymbol{\rho}}_n\cdot\hat{\boldsymbol{n}}\right)\hat{\boldsymbol{e}}_{TE}\\ &\quad + (1+R_{TE})\left[\boldsymbol{e}_i^{(-n)}(t)\cdot\hat{\boldsymbol{e}}_{TE}\right]\left(\hat{\boldsymbol{e}}_{TE}\times\hat{\boldsymbol{n}}\right) \qquad (19)\\ \boldsymbol{e}_i^{(-n)}(t) &= p^{(-n)}(t)*\mathbb{F}^{-1}\left[\boldsymbol{F}(\theta,\varphi)\right] \qquad (20)\\ \boldsymbol{h}_i^{(-n)}(t) &= \hat{\boldsymbol{\rho}}_n\times\boldsymbol{e}_i^{(-n)}(t) \qquad (21)\end{aligned}$$

If plate S is a plate of N-polygonal shape, based on Zhou's work in [7], the surface integral part in (16) and (17) can be written as the following closed-form representations:

if $\boldsymbol{\beta}=0$, then

$$\int_S\delta'\left(t-\frac{\left(\hat{\boldsymbol{\rho}}_n-\hat{\boldsymbol{R}}_n\right)\cdot\boldsymbol{r}'}{c}\right)dS' = \delta'\left(t-\frac{\boldsymbol{\omega}\cdot\boldsymbol{r}_n}{c}\right)\Delta S \qquad (22)$$

if $\boldsymbol{\beta}\neq 0$, then

$$\begin{aligned}\int_S\delta'\left(t-\frac{\left(\hat{\boldsymbol{\rho}}_n-\hat{\boldsymbol{R}}_n\right)\cdot\boldsymbol{r}'}{c}\right)dS' &= \frac{c}{|\boldsymbol{\beta}|^2}\sum_{i=0}^{N}\left(\boldsymbol{\omega}\times\hat{\boldsymbol{n}}\right)\\ &\quad\cdot(\boldsymbol{v}_{i+1}-\boldsymbol{v}_i)\\ &\begin{cases}\delta\left(t-\dfrac{\boldsymbol{\omega}\cdot\boldsymbol{v}_i}{c}\right) & \boldsymbol{\omega}\cdot(\boldsymbol{v}_{i+1}-\boldsymbol{v}_i)=0\\ \dfrac{c}{\boldsymbol{\omega}\cdot(\boldsymbol{v}_{i+1}-\boldsymbol{v}_i)}\left[\begin{array}{c}\varepsilon\left(t-\dfrac{\boldsymbol{\omega}\cdot\boldsymbol{v}_i}{c}\right)\\ -\varepsilon\left(t-\dfrac{\boldsymbol{\omega}\cdot\boldsymbol{v}_{i+1}}{c}\right)\end{array}\right] & \boldsymbol{\omega}\cdot(\boldsymbol{v}_{i+1}-\boldsymbol{v}_i)\neq 0\end{cases}\end{aligned} \qquad (23)$$

In the above equation, $\boldsymbol{\omega}=\hat{\boldsymbol{\rho}}_n-\hat{\boldsymbol{R}}_n$ and $\boldsymbol{\beta}$ is the projection of $\boldsymbol{\omega}$ on the polygonal surface. v_i and v_{i+1} represent the starting and ending position coordinates of the ith edge in the global coordinate respectively.

III. NEAR-FIELD SHOOTING AND BOUNCING RAYS

Consider that a ray tube launched from an antenna at position P radiates to triangle 0 and reflects to an area containing some triangle patches, as shown in Fig. 2. P_1 is the mirror image of P to triangle 0.

In order to determine which triangle is in the illuminated area, the following steps should be carried out.

First, connect P_1 to the center of triangle 0 to obtain the forward ray and the triangle patch (i.e., triangle 7) intersecting with the forward ray can be obtained by intersecting judgment. Second, we need to determine whether the three adjacent triangles (i.e., triangle 6, 8 and 13) of the triangle 7 are illuminated. Connect the center of adjacent triangle to P_1

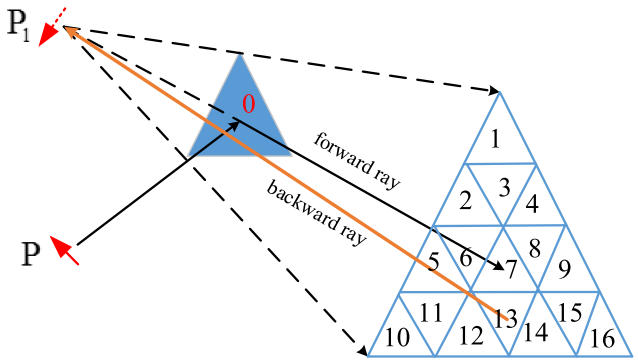

FIGURE 2. Intersection judgment between ray tube and triangle patches.

to obtain the backward ray. If the backward ray intersects the triangle 0, the adjacent triangle is illuminated. Thereafter, backward-ray-tracing process continues for these three adjacent triangles' adjacent triangles until some triangles outside the illuminated area occur.

After determining these triangles illuminated by reflected wave, the next work is to obtain the incident fields of these illuminated triangles. As shown in Fig. 3, triangle 1 is one of the triangle patches in illuminated area. $\boldsymbol{r}_0$ and $\boldsymbol{r}_1$ denote the points of triangle 0 and triangle 1, respectively. As discussed in the last section, the incident field on triangle 0 can be approximate a plane wave. According to Fresnel's law of reflection, the reflection fields on triangle 0 can be written as:

$$\begin{aligned}\boldsymbol{E}_0^r(\boldsymbol{r}_0,t) &= R_{TE}\left[\boldsymbol{E}_i(\boldsymbol{r}_0,t)\cdot\hat{\boldsymbol{e}}_{TE}\right]\hat{\boldsymbol{e}}_{TE}+R_{TM}\left[\boldsymbol{E}_i\right.\\ &\quad\left.\times\ (\boldsymbol{r}_0,t)\cdot\hat{\boldsymbol{e}}_{TM}\right]\left(\hat{\boldsymbol{e}}_{TE}\times\hat{\boldsymbol{\rho}}_1\right)\\ &= \frac{\eta}{4\pi\rho}p(t)*\mathbb{F}^{-1}\left[\boldsymbol{F}_1(\theta,\varphi)\right]*\delta\left(t-\frac{\rho}{c}\right) \quad (24)\\ \boldsymbol{H}_0^r(\boldsymbol{r}_0,t) &= R_{TE}\left[\boldsymbol{H}_i(\boldsymbol{r}_0,t)\cdot-\hat{\boldsymbol{e}}_{TM}\right]\left(\hat{\boldsymbol{\rho}}_1\times\hat{\boldsymbol{e}}_{TE}\right)+R_{TM}\\ &\quad\times\left[\boldsymbol{H}_i(\boldsymbol{r}_0,t)\cdot\hat{\boldsymbol{e}}_{TE}\right]\hat{\boldsymbol{e}}_{TE}\\ &= \frac{1}{\eta}\hat{\boldsymbol{\rho}}_1\times\boldsymbol{E}_0^r(\boldsymbol{r}_0,t) \quad (25)\end{aligned}$$

where

$$\boldsymbol{F}_1(\theta,\varphi)=\boldsymbol{F}(\theta,\varphi)\cdot\left[R_{TE}\hat{\boldsymbol{e}}_{TE}\hat{\boldsymbol{e}}_{TE}+R_{TM}\hat{\boldsymbol{e}}_{TM}\hat{\boldsymbol{e}}_{TE}\times\hat{\boldsymbol{\rho}}_1\right]$$

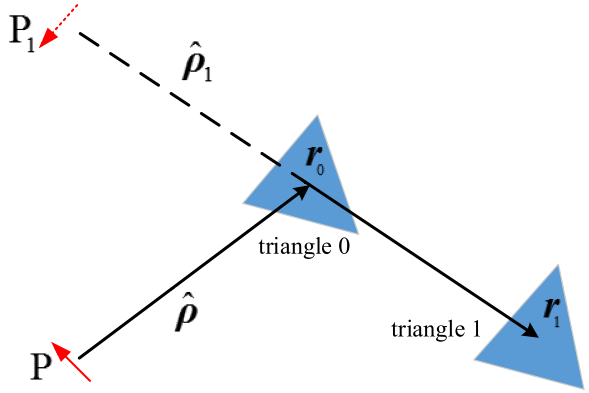

FIGURE 3. The incident field of the triangle patch is obtained by equivalent image antenna.

It can be seen from the reflection field expressions that the reflection fields can be regarded as the radiation fields from an equivalent image antenna at the point P_1 with $\boldsymbol{F}_1(\theta,\varphi)$. So the reflection fields received at $\boldsymbol{r}_1$ of triangle 1 can be substituted by the radiation fields from the equivalent image antenna at P_1. In other words, the incident fields of triangle 1 can be expressed as:

$$\boldsymbol{E}_1^i(\boldsymbol{r},t)=\frac{\eta}{4\pi\rho_1}p(t)*\mathbb{F}^{-1}\left[\boldsymbol{F}_1(\theta,\varphi)\right]*\delta\left(t-\frac{\rho_1}{c}\right) \quad (26)$$

$$\boldsymbol{H}_1^i(\boldsymbol{r},t)=\frac{1}{\eta}\hat{\boldsymbol{\rho}}_1\times\boldsymbol{E}_1^i(\boldsymbol{r},t) \quad (27)$$

Next, for the second triangle (triangle 2) that is illuminated by the ray reflected from triangle 1, it is easy to know that the equivalent image antenna position P_2 of triangle 2 is the mirror image of P_1 to triangle 1. And the $\boldsymbol{F}_2(\theta,\varphi)$ can be derived as

$$\boldsymbol{F}_2(\theta,\varphi)=\boldsymbol{F}_1(\theta,\varphi)\cdot\left[R_{TE}\hat{\boldsymbol{e}}_{TE}\hat{\boldsymbol{e}}_{TE}+R_{TM}\hat{\boldsymbol{e}}_{TM}\hat{\boldsymbol{e}}_{TE}\times\hat{\boldsymbol{\rho}}_2\right] \quad (28)$$

For the ith triangle (triangle i), the equivalent image antenna position P_i of triangle i is the mirror image of P_{i-1} to triangle i-1. And the $\boldsymbol{F}_i(\theta,\varphi)$ can be derived as

$$\boldsymbol{F}_i(\theta,\varphi)=\boldsymbol{F}_{i-1}(\theta,\varphi)\cdot\left[R_{TE}\hat{\boldsymbol{e}}_{TE}\hat{\boldsymbol{e}}_{TE}+R_{TM}\hat{\boldsymbol{e}}_{TM}\hat{\boldsymbol{e}}_{TE}\times\hat{\boldsymbol{\rho}}_i\right] \quad (29)$$

where $\hat{\boldsymbol{\rho}}_i$ is a unit vector pointing from P_i to the point on triangle i.

Repeat tracing the ray until no more reflection occurs. The incident fields of each small face can be substituted by the radiation fields from the equivalent image antenna. The scattering fields of each face can be evaluated by using TDPO proposed in last section. And the total fields can be obtained by adding the scattering fields of all faces shot by ray tubes.

IV. NUMERICAL EXAMPLES

In this section, several numerical examples are given to validate both the accuracy and efficiency of the proposed TDSBR method. The surface of target is meshed into flat triangular facets. The frequency domain SBR is referring to as FDSBR. The fast Fourier transform (FFT) will be used to convert the transient results to frequency domain, and the inverse fast Fourier transform (IFFT) for the opposite direction. In order to prove the accuracy of this TDSBR method, we also give some full wave results obtained by the multilevel fast multipole algorithm (MLFMA) of commercial software FEKO. In order to compare the computation time, all the simulation results are obtained on the same desktop computer.

We choose the third-order derivative of a modulated Gaussian pulse as the excitation pulse of the antenna. The excitation pulse can be expressed by

$$p(t)=\frac{d^3}{dt^3}\left\{\cos\left[2\pi f_0(t-t_0)\right]\exp\left[-4\pi\frac{(t-t_0)^2}{\tau^2}\right]\right\} \quad (30)$$

Let f_0 denote the center frequency in the spectrum of modulated Gaussian pulse and f_b denote the frequency bandwidth. In the above excitation pulse expression, $\tau = 4/f_b$. t_0 is a time offset. In the following simulations, $f_0 = 8\text{GHz}$, $f_b = 4\text{GHz}$, and $t_0 = \tau$ are set.

A. DIPOLE SOURCE

At first, the scattering of a PEC trihedral corner reflector with a side length of 0.3 m illuminated by a dipole source is considered to validate both the accuracy and efficiency of the proposed TDSBR method. The vector current moment $\boldsymbol{f}(\theta, \varphi)$ of the dipole antenna is given by

$$\boldsymbol{f}(\theta, \varphi) = Il\hat{\boldsymbol{\rho}} \times \left(\hat{\boldsymbol{l}} \times \hat{\boldsymbol{\rho}}\right) \tag{31}$$

and

$$\begin{aligned}\mathbb{F}^{-1}\left[\boldsymbol{F}(\theta, \varphi)\right] &= \mathbb{F}^{-1}\left[-jk\boldsymbol{f}(\theta, \varphi)\right] \\ &= -\hat{\boldsymbol{\rho}} \times \left(\hat{\boldsymbol{l}} \times \hat{\boldsymbol{\rho}}\right) \frac{Il}{c}\delta'(t)\end{aligned} \tag{32}$$

so, the transient radiation fields of the dipole antenna with excitation pulse $p(t)$ can be given by

$$\begin{aligned}\boldsymbol{E_i}\left(\boldsymbol{r'}, t\right) &= \frac{\eta}{4\pi\rho} p(t) * \mathbb{F}^{-1}\left[-jk\boldsymbol{f}(\theta, \varphi)\right] * \delta\left(t - \frac{\rho}{c}\right) \\ &= -\hat{\boldsymbol{\rho}} \times \left(\hat{\boldsymbol{l}} \times \hat{\boldsymbol{\rho}}\right) \frac{\eta Il}{4\pi\rho c} p'\left(t - \frac{\rho}{c}\right)\end{aligned} \tag{33}$$

The dipole antenna is located at $r_i = 3\ m$, $\theta_i = 45°$, and $\varphi_i = 45°$. And $\hat{\boldsymbol{l}} = \hat{\boldsymbol{\varphi}}$, $Il = 1\text{A} \cdot \text{m}$. In order to improve the accuracy of the ray tracing algorithm and satisfy the far-field approximation condition, the trihedral corner reflector is dispersed into 3066 small triangles with an average size of $\lambda_{\min}/3$. Fig. 4(a) compares the φ-polarized transient monostatic scattering electric fields by TDSBR and FDSBR with IFFT, as well as the results obtained by the MLFMA of FEKO in conjunction with IFFT. Fig. 4 (c) presents the corresponding normalized wideband results in frequency domain. As we can see in Fig. 4 (a) and (c), the results of TDSBR and FDSBR agree well but slightly different from MLFMA. There are two main reasons for this error. First of all, this major error is caused by high frequency approximation of SBR. Compared with the numerical algorithm, there must be some errors. The second reason is that the scattering field of the surface only contains PO field, and the diffraction contribution of the surface edge (such as diffraction physics theory) is not considered.

In the second case, we simulate the scattering near field of a quasi-real metallic ship model to further verify the accuracy of the proposed method. The size of the ship model is 0.9 m × 0.2 m × 0.2 m. The ship is dispersed into 12588 triangles with an average size of $\lambda_{\min}/3$. The dipole antenna is located at (0, 0, 5) m. And $\hat{\boldsymbol{l}} = \hat{\boldsymbol{\varphi}}$, $Il = 1\text{A} \cdot \text{m}$. Fig. 4 (b) shows the φ-polarized transient monostatic scattering electric field simulated by TDSBR, and compares the result with that of FDSBR-IFFT and MLFMA-IFFT. And the corresponding normalized wideband result are compared in Fig. 4 (d). As can be seen from the Fig. 4 (b) and (d), the results of TDSBR and FDSBR are in good agreement, and slight differences are found by comparing with MLFMA.

TABLE 1 gives the triangle numbers (by subdividing the surface of target) and computation time between the TDSBR and MLFMA. The IFFT process is not included in the calculation cost of MLFMA-IFFT. It is worth noting that since the ship is a closed body, the combined integral equation technique is used in MLFMA to improve the simulation efficiency. For trihedral corner reflector, the electric field integral equation is used in MLFMA. Compared with the electric field integral equation, the combined integral equation converges faster. Therefore, although the ship has more triangular patches than the trihedral corner reflector, the calculation time is greatly reduced due to the use of combined integral equation technique. As shown in the table, the ratio of the number of patches of TDSBR to that of MLFMA is about 1:7, and the ratio of the computation time is approximately 1:1096 for the trihedral corner reflector and 1:1407 for the simple ship.

TABLE 1. Patch number and computation times comparison between tdsbr and mlfma-ifft for the trihedral corner reflector.

	Number of patches		Computation time (s)	
	Fig.4(a)	Fig.4(b)	Fig.4(a)	Fig.4(b)
TDSBR	3066	12588	15.05	20.87
FDSBR-IFFT	3066	12588	30.97	45.68
MLFMA-IFFT	22053	90092	16507.95	29373.40

As the third case, the monostatic scattering results versus incident angle θ_i and the bistatic scattering results versus observation angle θ_s are investigated. The definitions of r_i, θ_i, φ_i, r_s,θ_s and φ_s are the same as in Fig. 4 (c). Fig. 5 and Fig. 6 show the normalized amplitudes of monostatic scattering electric fields and bistatic scattering electric fields of the metallic simple ship illuminated by a half-wave dipole antenna, respectively. The result of TDSBR is obtained from the wideband results at f = 8 GHz. In Fig. 5, the antenna is on a circle of radius $r = 5\ m$ centered at the origin on the $\varphi_i = 0°$ plane and θ_i ranges from -90° to 90°. In Fig. 6, the transmitting antenna is located at (0, 0, 5) m, and the receiving antenna is on a circle of radius $r = 5\ m$ centered at the origin on the $\varphi_i = 0°$ plane and θ_s ranges from $-90°$ to 90°. As shown in these figures, the results of TDSBR and FDSBR are in good agreement. In addition to the errors caused by the high frequency approximation, the difference with MLFMA is due to the fact that the ship has a lot of edge diffraction and the calculation of diffraction field is not considered in SBR method. As shown in Fig. 5, due to there are more edge diffraction on the ship's bow, so the error between TDSBR and MLFMA is obvious when the antenna illuminates the ship's bow ($\theta_i > 0°$).

B. DIPOLE ARRAY

In the next example, we consider the near field scattering where the radiation antenna is a dipole array. Consider a dipole array of N elements, pointing in the $\hat{\boldsymbol{l}}$ direction and placed along the $\hat{\boldsymbol{d}}$ direction with equal spacing d. The phase shift between adjacent elements is α. The current amplitude

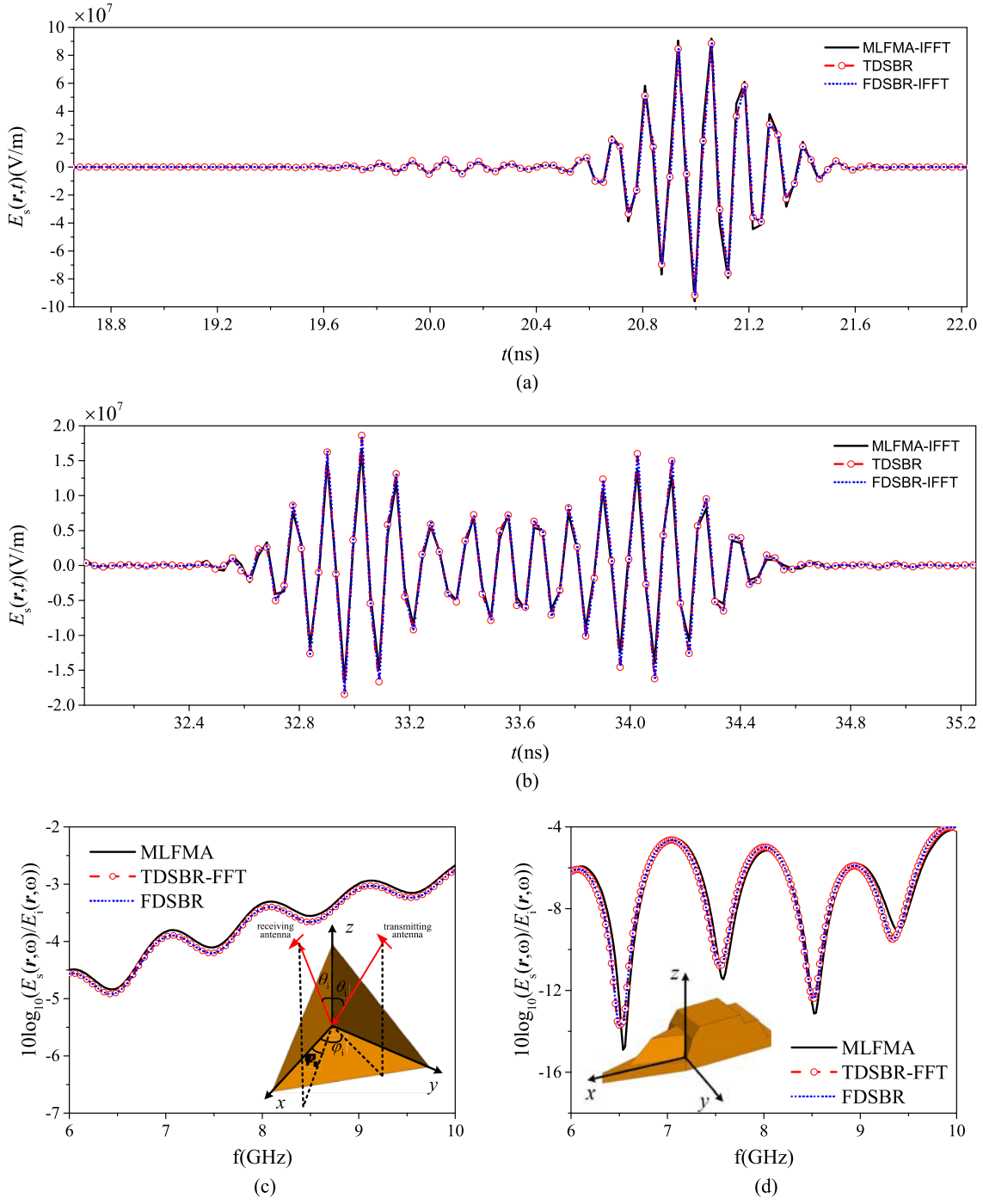

FIGURE 4. (a) and (c) Monostatic scattering electric fields from a PEC trihedral corner reflector illuminated by a half-wave dipole antenna. (a) Transient result and (c) normalized wideband result. (b) and (d) Monostatic scattering electric fields from a quasi-real metallic ship illuminated by a half-wave dipole antenna. (b) Transient result and (d) normalized wideband result.

is I_n. The vector current moment $\boldsymbol{f}(\theta, \varphi)$ of such a dipole array can be expressed as [25]:

$$\begin{aligned}\boldsymbol{f}(\theta,\varphi) &= l\hat{\boldsymbol{\rho}}\times\left(\hat{\boldsymbol{l}}\times\hat{\boldsymbol{\rho}}\right)\sum_{n=0}^{N-1} I_n \exp\left[jn\left(kd\sin\theta\cos\varphi-\alpha\right)\right] \\ &= l\hat{\boldsymbol{\rho}}\times\left(\hat{\boldsymbol{l}}\times\hat{\boldsymbol{\rho}}\right)\sum_{n=0}^{N-1} I_n \exp\left[jn\left(kd\cos\psi-\alpha\right)\right] \quad (34)\end{aligned}$$

and

$$\begin{aligned}\mathbb{F}^{-1}\left[\boldsymbol{F}(\theta,\varphi)\right] &= \mathbb{F}^{-1}\left[-jk\boldsymbol{f}(\theta,\varphi)\right] \\ &= -\hat{\boldsymbol{\rho}}\times\left(\hat{\boldsymbol{l}}\times\hat{\boldsymbol{\rho}}\right)\frac{l}{c} \\ &\quad\times\sum_{n=0}^{N-1}\left[I_n\exp\left(-jn\alpha\right)\delta'\left(t+\frac{nd\cos\psi}{c}\right)\right] \quad (35)\end{aligned}$$

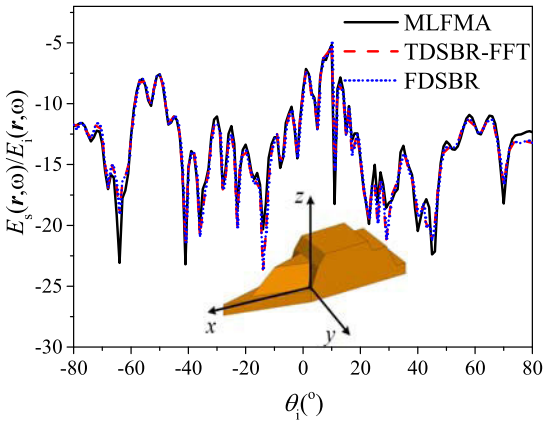

FIGURE 5. Normalized amplitudes of monostatic scattering electric fields from a simple metallic ship as a function of the incident angle θ_i.

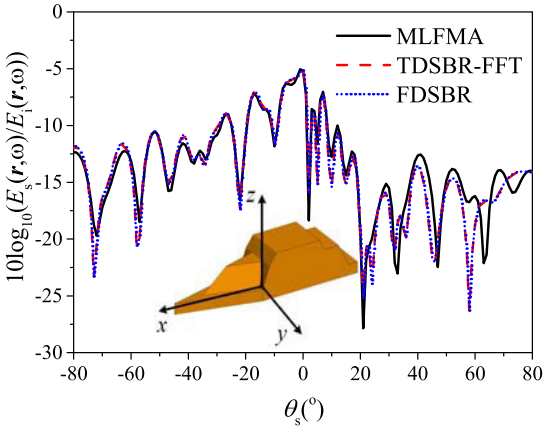

FIGURE 6. Normalized amplitudes of bistatic scattering electric fields from a simple metallic ship as a function of the observation angle θ_s.

According to (3), the transient radiation fields of the dipole array with excitation pulse $p(t)$ can be given by

$$\begin{aligned}\boldsymbol{E_i}(\boldsymbol{r'},t) &= \frac{\eta}{4\pi\rho}p(t) * \mathbb{F}^{-1}\left[-jk\boldsymbol{f}(\theta,\varphi)\right] * \delta\left(t-\frac{\rho}{c}\right)\\ &= -\hat{\boldsymbol{\rho}}\times\left(\hat{\boldsymbol{l}}\times\hat{\boldsymbol{\rho}}\right)\frac{\eta l}{4\pi\rho c}\\ &\quad\times\sum_{n=0}^{N-1}\left[I_n\exp\left(-jn\alpha\right)p'\left(t-\frac{\rho}{c}+\frac{nd\cos\psi}{c}\right)\right]\end{aligned} \tag{36}$$

We consider the near-field scattered electric field from the quasi-real metallic ship model illuminated by a dipole array with 7 elements ($N = 7$) (Fig. 7). The center of the dipole array is at (0, 0, 20) m. The elements are placed along the $\hat{\boldsymbol{x}}$ axis. $\hat{\boldsymbol{l}} = \hat{\boldsymbol{y}}$, $\alpha = 0$, $lI_n = 1\text{A}\cdot m$ and $d = \lambda_0/2$. λ_0 is the wavelength corresponding to the center frequency f_0.

Fig. 8(a) shows the φ-polarized transient scattering electric fields at (0, 0, 5) m simulated by TDSBR, and compares the result with that of FDSBR-IFFT and MLFMA-IFFT. The line marked as absolute error represents the absolute error value

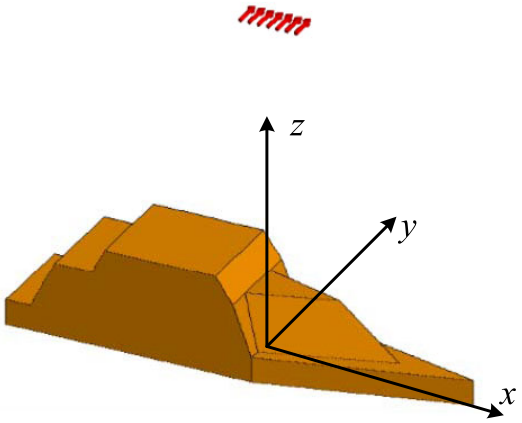

FIGURE 7. A dipole array irradiates the quasi-real metallic ship model.

between TDSBR and MLFMA-IFFT. The corresponding normalized wideband result are compared in Fig. 8(b). As can be seen from the Fig. 8(a), the echo is mainly divided into two parts. The early echo is mainly from the scattering of the plate in the middle of the ship and the echo in the later period mainly comes from the scattering of the prow and stern. The results of TDSBR and FDSBR are in good agreement during the entire echo period. The correlation coefficient between TDSBR and FDSBR-IFFT is 0.99897. The maximum of absolute error is 6.99×10^6 at $t = 84.06$ ns and the relative error is 0.49. Since there are many edge diffraction in prow and stern, compared with MLFMA method, the error mainly appears in the later period of the echo. The correlation coefficient between TDSBR and MLFMA-IFFT is 0.98139.

C. LINEAR ANTENNA

Finally, we consider the transient scattering from a complex ship illuminated by a linear antenna. Consider a linear antenna with a length of L, pointing in the $\hat{\boldsymbol{l}}$ direction. The vector current moment $\boldsymbol{f}(\theta,\varphi)$ of such a linear antenna can be expressed as [25]

$$\boldsymbol{f}(\theta,\varphi) = \hat{\boldsymbol{\rho}}\times\left(\hat{\boldsymbol{l}}\times\hat{\boldsymbol{\rho}}\right)\frac{2I_0}{k\sin\theta}\left[\cos\left(\frac{kl}{2}\cos\theta\right)-\cos\left(\frac{kl}{2}\right)\right] \tag{37}$$

and

$$\begin{aligned}\mathbb{F}^{-1}\left[\boldsymbol{F}(\theta,\varphi)\right] &= \mathbb{F}^{-1}\left[-jk\boldsymbol{f}(\theta,\varphi)\right]\\ &= \left\{-\hat{\boldsymbol{\rho}}\times\left(\hat{\boldsymbol{l}}\times\hat{\boldsymbol{\rho}}\right)\frac{jI_0}{\sin\theta}\left[\delta\left(t-\frac{L\cos\theta}{2c}\right)\right.\right.\\ &\quad+\delta\left(t+\frac{L\cos\theta}{2c}\right)-\delta\left(t-\frac{L}{2c}\right)\\ &\quad\left.\left.-\delta\left(t+\frac{L}{2c}\right)\right]\right\}\end{aligned} \tag{38}$$

According to (3), the transient radiation fields of the linear antenna with excitation pulse $p(t)$ can be

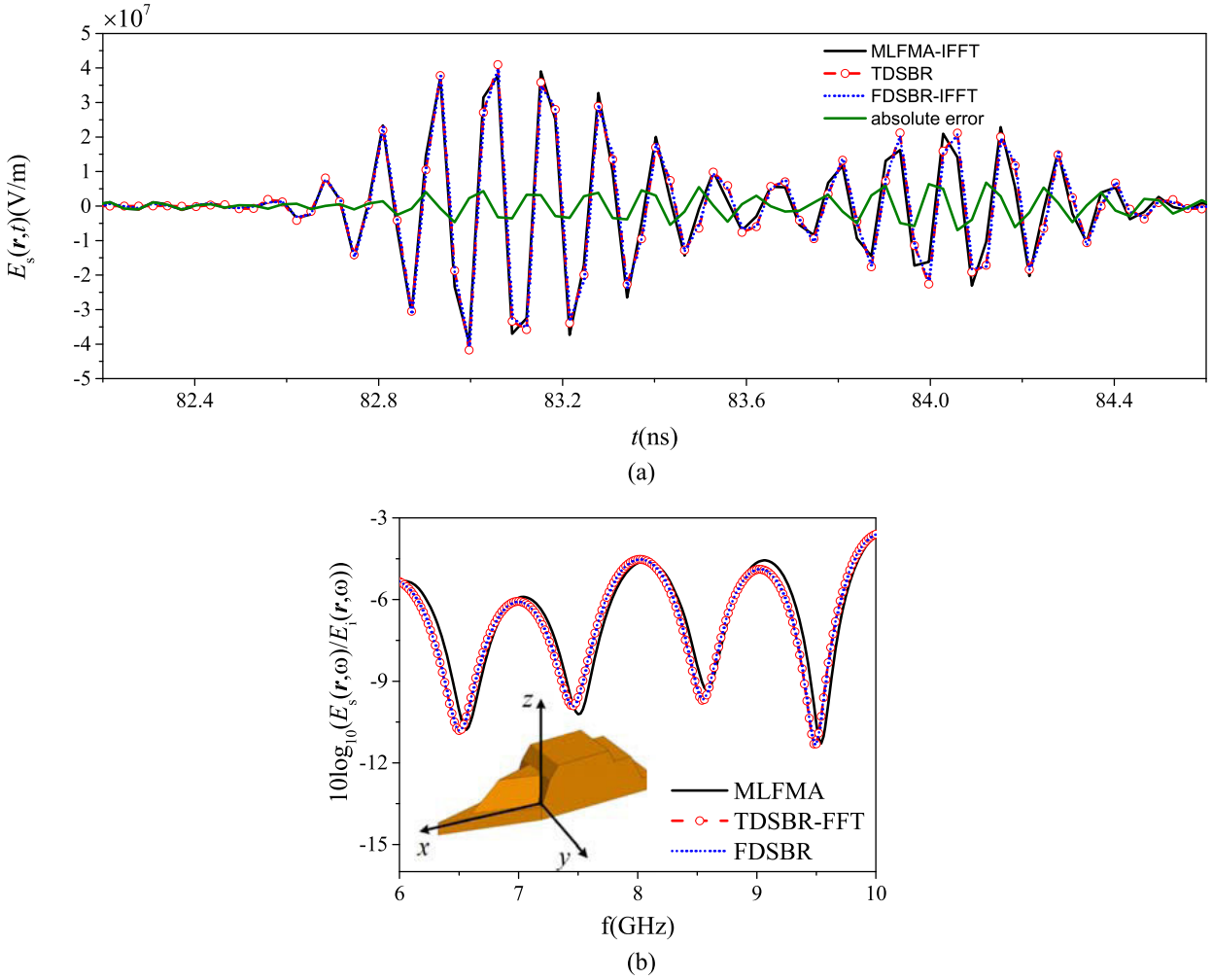

FIGURE 8. Scattering electric fields from a PEC trihedral corner reflector illuminated by a dipole array. (a) Transient result and (b) normalized wideband result.

given by

$$\begin{aligned}\boldsymbol{E_i}\left(\boldsymbol{r'},t\right) &= \frac{\eta}{4\pi\rho}p\left(t\right)*\mathbb{F}^{-1}\left[-jk\boldsymbol{f}\left(\theta,\varphi\right)\right]*\delta\left(t-\frac{\rho}{c}\right)\\ &= \frac{\eta}{4\pi\rho}p\left(t-\frac{\rho}{c}\right)*\left\{-\hat{\boldsymbol{\rho}}\times\left(\hat{\boldsymbol{l}}\times\hat{\boldsymbol{\rho}}\right)\frac{jI_0}{\sin\theta}\right.\\ &\quad\times\left[\delta\left(t-\frac{L\cos\theta}{2c}\right)+\delta\left(t+\frac{L\cos\theta}{2c}\right)\right.\\ &\quad\left.\left.-\delta\left(t-\frac{L}{2c}\right)-\delta\left(t+\frac{L}{2c}\right)\right]\right\}\end{aligned}\tag{39}$$

In the following simulation, we set $L=\lambda_0/2$ and $\hat{\boldsymbol{l}}=\hat{\boldsymbol{\varphi}}$. The dimension of the ship is about 15 m × 1.8 m × 3 m. The ship is dispersed into 51208 triangles with an average size of 0.06 m.

Fig. 9(a) compares the φ-polarized transient monostatic scattering electric fields by TDSBR and FDSBR with IFFT. Fig. 9 (b) compares the φ-polarized transient bistatic scattering electric fields by TDSBR and FDSBR with IFFT. Since the distance between different parts of the ship and the antenna is different, the scattering contribution will arrive at the observation point at different times. Therefore, the total scattering field will be separated into multiple parts in time. As can be seen, the transient results are in perfect agreement between the two approaches.

Then we analyze the variation of scattering field with distance. Define the near-field RCS (NFRCS) as:

$$\text{NFRCS}=20\log_{10}\left(2\sqrt{\pi}r\left|\boldsymbol{E}^s\left(\boldsymbol{r}\right)\right|\Big/\left|\boldsymbol{E}^i\left(-\boldsymbol{r}_s\right)\right|\right)\tag{40}$$

Fig. 10-12 show the transient scattering field and normalized wideband NFRCS of the ship as a function of distance r_i under the radiations of dipole antenna, dipole array and linear antenna, separately. For the sake of illustration in figures, the initial time of transient scattering field is shifted to t = 0. As shown in these figures, with the change of distance, the scattering field of the target presents different characteristics. When the antenna is located in the near region of the target, the scattering field changes irregularly, which is the near region scattering characteristic. With the increase of the distance r_i, the scattering characteristics gradually

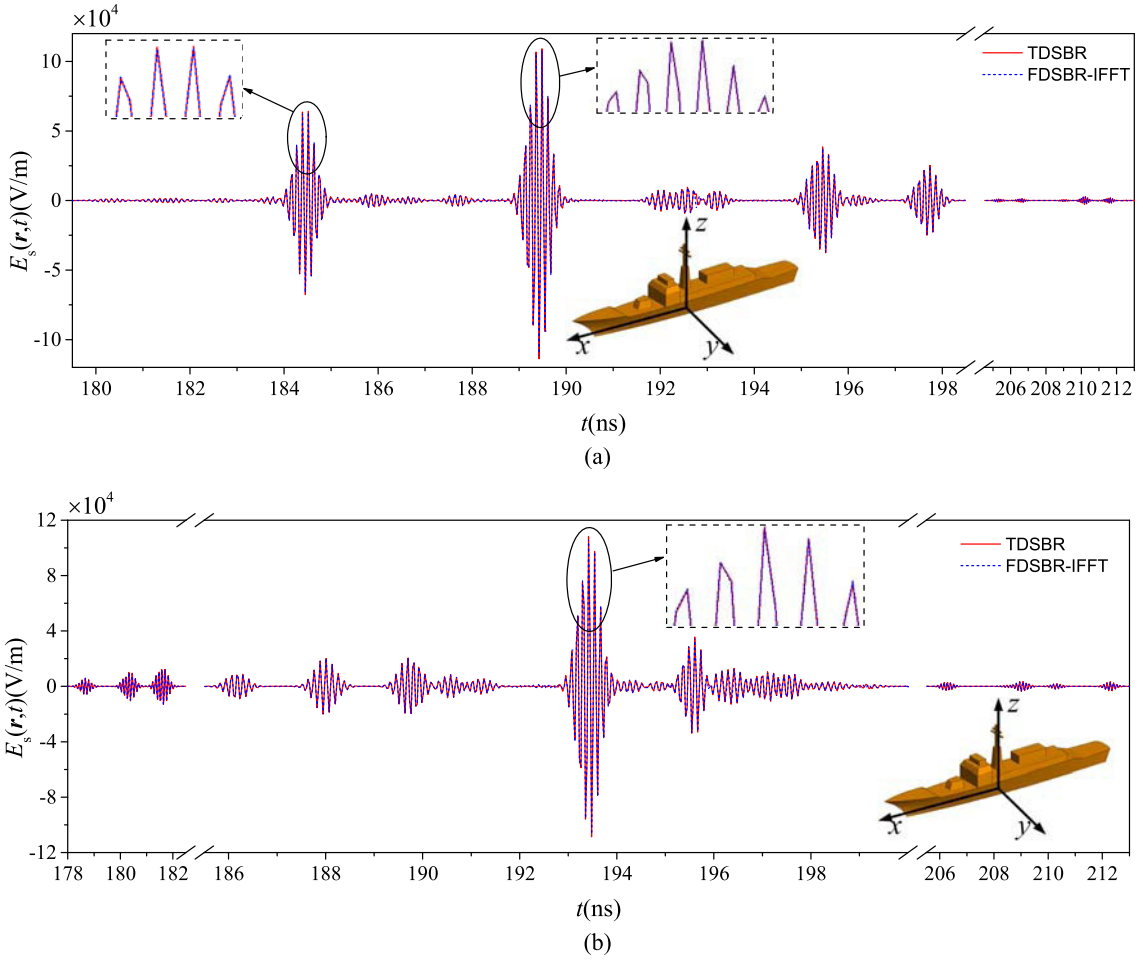

FIGURE 9. Scattered electric fields from a complex metallic ship illuminated by a linear antenna. (a) Monostatic scattering at (r_i, θ_i, φ_i) = (30 m, 30°, 0°). (b) Bistatic scattering of (r_i, θ_i, φ_i) = (30 m, 30°, 0°) and (r_s, θ_s, φ_s) = (30 m, 30°, 180°).

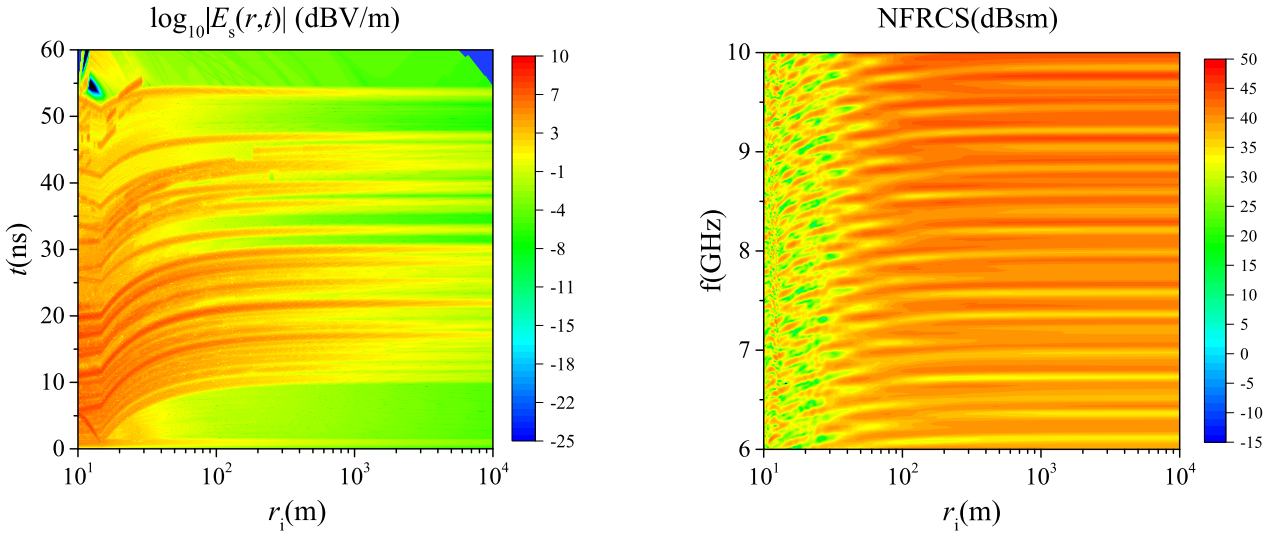

FIGURE 10. Backscattering characteristic as a function of the distance r_i under radiation of a dipole antenna at (θ_i, φ_i) = (30°, 0°). (a) Transient result and (b) normalized wideband NFRCS.

become stable, that is, the far-field scattering characteristics begin to appear. The width and envelope characteristics of the transient scattering pulse remain stable on the whole, and only the amplitude decreases as the distance increases. And the NFRCS also gradually approaches a stable value, that is, the far-field RCS.

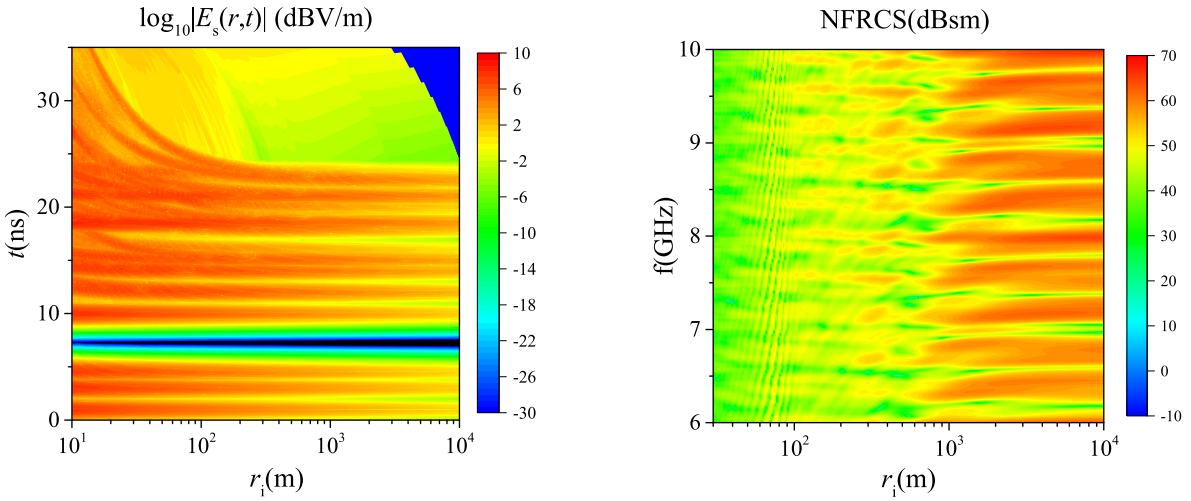

FIGURE 11. Backscattering characteristic as a function of the distance r_i under radiation of a dipole array at $(\theta_i, \varphi_i) = (0°, 0°)$. (a) Transient result and (b) normalized wideband NFRCS.

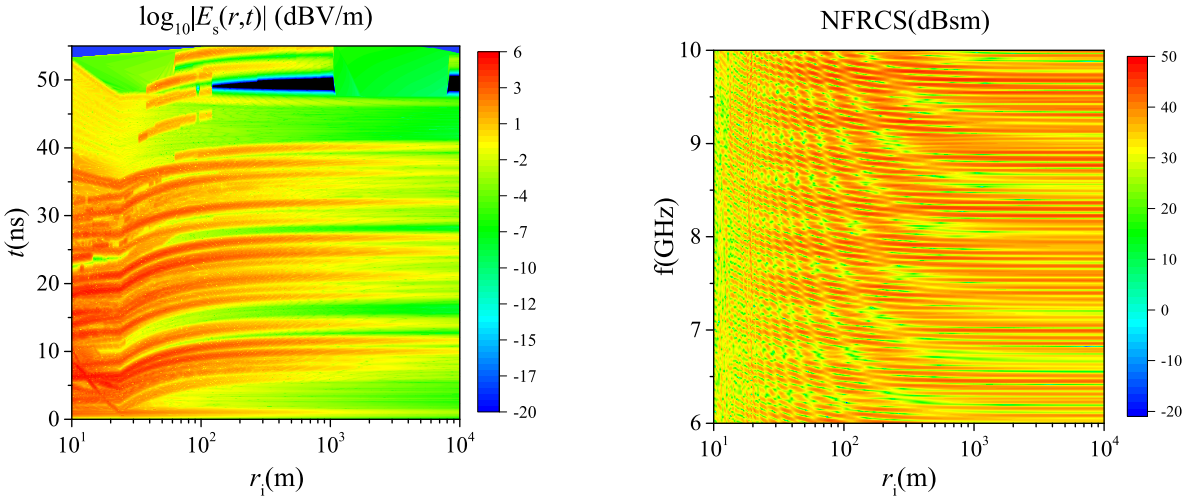

FIGURE 12. Backscattering characteristic as a function of the distance r_i under radiation of a linear antenna at $(\theta_i, \varphi_i) = (30°, 0°)$. (a) Transient result and (b) normalized wideband NFRCS.

V. CONCLUSION

This paper proposed an efficient time domain shooting and bouncing ray (TDSBR) method to analyze the transient near-field scattering from electrically large complex objects illuminated by a far-field antenna source. The closed-form TDPO near-field expressions are derived by applying locally expanded Green function approximation. The incident fields of each individual facet in the ray path is represented by the radiation fields from the equivalent image antenna. Numerical analyses show that the proposed method performs good accuracy for the analysis of near-field transient scattering problem when compared with the MLFMA. The TDSBR is applicable to analyze the near-field scattering problem of a target illuminated by an arbitrary far-field source as long as the impulse response of the antenna radiation field is available. Compared with FD method, TD method has the biggest advantage that the transient scattering echoes are closer to the actual radar detection echoes and the transient scattered echoes can be directly used in echo processing, such as SAR imaging. The further work is to combine TDSBR and SAR imaging and carry out SAR imaging research based on transient scattering echo.

REFERENCES

[1] K. S. Kunz and K.-M. Lee, "A three-dimensional finite-difference solution of the external response of an aircraft to a complex transient EM environment: Part II-comparison of predictions and measurements," *IEEE Trans. Electromagn. Compat.*, vol. EMC-20, no. 2, pp. 333–341, May 1978.

[2] S. M. Rao and D. R. Wilton, "Transient scattering by conducting surfaces of arbitrary shape," *IEEE Trans. Antennas Propag.*, vol. 39, no. 1, pp. 56–61, Jan. 1991.

[3] E.-Y. Sun and W. V. T. Rusch, "Time-domain physical-optics," *IEEE Trans. Antennas Propag.*, vol. 42, no. 1, pp. 9–15, Jan. 1994.

[4] W. B. Gordon, "Far-field approximations to the Kirchoff-Helmholtz representations of scattered fields," *IEEE Trans. Antennas Propag.*, vol. AP-23, no. 4, pp. 590–592, Jul. 1975.

[5] X. Zhou and T. J. Cui, "A closed-form representation of time-domain far fields based on physical optics," *IEEE Antennas Wireless Propag. Lett.*, vol. 11, pp. 965–968, 2012.
[6] S. R. Legault, "Refining physical optics for near-field computations," *Electron. Lett.*, vol. 40, no. 1, pp. 71–72, Jan. 2004.
[7] X. Zhou and T. J. Cui, "Efficient evaluation of near-field time-domain physical-optics integral using locally expanded green function approximation," *Prog. Electromagn. Res.*, vol. 150, pp. 41–48, 2015.
[8] T. T. Fan, X. Zhou, W. M. Yu, X. Y. Zhou, and T. J. Cui, "Time-domain line-integral representations of physical-optics scattered fields," *IEEE Trans. Antennas Propag.*, vol. 65, no. 1, pp. 309–318, Jan. 2017.
[9] T. Whitted, "An improved illumination model for shaded display," *Commun. ACM*, vol. 23, no. 6, pp. 343–349, Jun. 1980.
[10] S. M. Rubin and T. Whitted, "A 3-dimensional representation for fast rendering of complex scenes," *Comput. Graph.*, vol. 14, no. 3, pp. 110–116, Jul. 1980.
[11] H. Ling, R.-C. Chou, and S.-S. Lee, "Shooting and bouncing rays: Calculating the RCS of an arbitrarily shaped cavity," *IEEE Trans. Antennas Propag.*, vol. 37, no. 2, pp. 194–205, Feb. 1989.
[12] S. Suk, T.-I. Seo, H.-S. Park, and H.-T. Kim, "Multiresolution grid algorithm in the SBR and its application to the RCS calculation," *Microw. Opt. Technol. Lett.*, vol. 29, no. 6, pp. 394–397, Jun. 2001.
[13] K. S. Jin, T.-I. Suh, S.-H. Suk, B.-C. Kim, and H.-T. Kim, "Fast ray tracing using a space-division algorithm for RCS prediction," *J. Electromagn. Waves Appl.*, vol. 20, no. 1, pp. 119–126, 2006.
[14] J.-K. Bang, B.-C. Kim, S.-H. Suk, B.-C. Kim, and H.-T. Kim, "Time consumption reduction of ray tracing for Rcs prediction using efficient grid division and space division algorithms," *J. Electromagn. Waves Appl.*, vol. 21, no. 6, pp. 829–840, Jan. 2007.
[15] T.-Q. Fan and L.-X. Guo, "OpenGL-based hybrid GO/PO computation for RCS of electrically large complex objects," *IEEE Antennas Wireless Propag. Lett.*, vol. 13, pp. 666–669, 2014.
[16] T.-Q. Fan, L.-X. Guo, B. Lv, and W. Liu, "An improved backward SBR-PO/PTD hybrid method for the backward scattering prediction of an electrically large target," *IEEE Antennas Wireless Propag. Lett.*, vol. 15, pp. 512–515, 2016.
[17] S.-K. Jeng, "Near-field scattering by physical theory of diffraction and shooting and bouncing rays," *IEEE Trans. Antennas Propag.*, vol. 46, no. 4, pp. 551–558, Apr. 1998.
[18] G. B. Guo and L. X. Guo, "SBR method for near-field scattering of an electrically large complex target illuminated by dipole sources," *IEEE Access*, vol. 6, pp. 78710–78718, 2018.
[19] H. Ling and R. Bhalla, "Time-domain ray-tube integration formula for the shooting and bouncing ray technique," Univ. Texas, Austin, TX, USA, Tech. Rep., Apr. 1993.
[20] R. Bhalla and H. Ling, "Image domain ray tube integration formula for the shooting and bouncing ray technique," *Radio Sci.*, vol. 30, no. 5, pp. 1435–1446, Sep./Oct. 1995.
[21] X. Zhou, J. Y. Zhu, W. M. Yu, and T. J. Cui, "Time-domain shooting and bouncing rays method based on beam tracing technique," *IEEE Trans. Antennas Propag.*, vol. 63, no. 9, pp. 4037–4048, Sep. 2015.
[22] P. S. Heckbert and P. Hanrahan, "Beam tracing polygonal objects," *SIGGRAPH Comput. Graph.*, vol. 18, no. 3, pp. 119–127, Jul. 1984.
[23] H. G. Park, H.-T. Kim, and K.-T. Kim, "Beam tracing for fast RCS prediction of electrically large targets," *Progr. Electromagn. Res. M*, vol. 20, pp. 29–42, 2011.
[24] Y. B. Tao, H. Lin, and H. J. Bao, "Adaptive aperture partition in shooting and bouncing ray method," *IEEE Trans. Antennas Propag.*, vol. 59, no. 9, pp. 3347–3357, Sep. 2011.
[25] J. A. Kong, *Electromagnetic Wave Theory*. New York, NY, USA: Wiley, 1986.
[26] T. B. Hansen and A. D. Yaghjian, *Plane-Wave Theory of Time-Domain Fields: Near-Field Scanning Applications*. New York, NY, USA: IEEE Press, 1999.

GUANGBIN GUO received the B.S. degree in electronic information science and technology from Xidian University, Xi'an, China, in 2015, where he is currently pursuing the Ph.D. degree in radio science with the School of Physics and Optoelectronic Engineering, Institute of Radio Propagation. His research interests include applied and computational electromagnetics for remote sensing from target above or below random rough surfaces.

LIXIN GUO (S'95–M'03–SM'16) received the M.S. degree in radio science from Xidian University, Xi'an, China, in 1993, and the Ph.D. degree in astrometry and celestial mechanics from the Chinese Academy of Sciences, China, in 1999.

From 2001 to 2002, he was a Visiting Scholar with the School of Electrical Engineering and Computer Science, Kyungpook National University, Daegu, South Korea. He has been a Visiting Professor with the d'Energetique des Systemes et Precedes (LESP), University of Rouen, Mont-Saint-Aignan, France, and the Faculty of Engineering and Physical Sciences, University of Manchester, Manchester, U.K. He has been a Chief Professor of Innovative Research Team in Shaanxi, China, since 2014. He is currently a Professor and the Head of the School of Physics and Optoelectronic Engineering, Xidian University, China. He has authored or coauthored four books and more than 300 journal papers. He has been in charge of and undertaken more than 30 projects. His research interests include electromagnetic wave propagation and scattering in complex and random media, computational electromagnetics, inverse scattering, and antenna analysis and design. He was a recipient of the National Science Fund for Distinguished Young Scholars, in 2012, and a Distinguished Professor of Changjiang Scholars Program, in 2014.

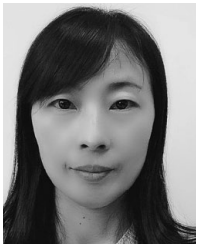

RUI WANG was born in Heyang, China, in 1981. She received the B.S. degree in electronic information science and technology and the Ph.D. degree in radio science from Xidian University, Xi'an, China, in 2004 and 2009, respectively. Her research interests include electromagnetic wave propagation and scattering in complex and random media, and computational electromagnetics for remote sensing from target above or below random rough surfaces.